J Solid State Electrochem (2012) 16:1975–1982
DOI 10.1007/s10008-011-1590-6

ORIGINAL PAPER

Synthesis, characterization, and biosensing application of ZnO/SnO_2 heterostructured nanomaterials

Rong Wu · Xiaohua Chen · Jianqiang Hu

Received: 29 May 2011 / Revised: 23 October 2011 / Accepted: 6 November 2011 / Published online: 2 December 2011

Abstract In this work, zinc oxide/tin oxide (ZnO/SnO_2) heterostructured nanomaterials were synthesized by hydrothermal method. Transmission electron microscopy, scanning electron microscopy, energy-dispersive X-ray spectroscopy, and X-ray diffraction measurements revealed that the product was composed of ZnO nanowires and SnO_2 nanobranches. The novel ZnO/SnO_2 heterostructured nanocrystals were for the first time used as a supporting matrix to explore a novel immobilization and biosensing platform of redox proteins. UV–visible absorption investigation indicated that hemoglobin (Hb) intercalated well in the ZnO/SnO_2 heterostructured nanocrystals retained its native structure. Comparative experiments have confirmed that the ZnO/SnO_2-based biosensor not only had enhanced direct electron transfer capacity but also displayed excellent electrocatalytic properties such as higher sensitivity and wider linear range to the detection of hydrogen peroxide in comparison with the ZnO- and SnO_2-based biosensors.

Keywords Zinc oxide (ZnO) and tin oxide (SnO_2) · Heterostructured nanomaterial · Direct electrochemistry · Electrocatalysis · Hemoglobin · Biosensor

R. Wu and X. Chen contributed equally to this work.

R. Wu · X. Chen · J. Hu (✉)
Key Lab for Fuel Cell Technology of Guangdong Province, Department of Applied Chemistry, College of Chemistry and Chemical Engineering, South China University of Technology, Guangzhou 510640, China
e-mail: jqhusc@scut.edu.cn

J. Hu
State Key Laboratory of Pulp and Paper Engineering, South China University of Technology, Guangzhou 510640, China

Introduction

One-dimensional (1D) nanostructures, such as nanorods, nanowires, nanotubes, and nanobelts, are attractive building blocks for the construction of electronic and optoelectronic device systems (e.g., sensors, laser diodes, field-effect transistors, and light-emitting diodes) [1–4]. To date, much effort has been focused on the integration of 1D nanoscale building blocks into 2D and 3D ordered superstructures or complex functional architectures, which is a crucial step toward the realization of functional nanoscale systems [5]. Tin oxide (SnO_2), an important *n*-type wide band-gap semiconductor (E_g=3.6 eV), is of potential applicability as transparent electrodes, gas sensors, information storage, and solar cells [6–8]. Although the sizes and morphologies of 1D SnO_2 nanomaterials could have been well controlled [9–12], synthesis of 1D SnO_2 nanomaterials with heterostructured nanocrystals through coupling other component nanomaterials is still rarely studied.

Heterostructured nanocrystals, in which the primary stems (or trunks) and the branches consist of different nanomaterials, offer an effective approach to increase structural complexity and acquire objective properties [12]. Therefore, it is of key importance for the realization of multifunctional nanodevices to control composition, size, and morphology of hierarchical building blocks in a predictable manner during synthesis [13]. ZnO and SnO_2, as well-known wide direct band-gap semiconductors, have been considered as the most promising functional materials due to their highly sensitive gas sensing and excellent optical properties [14, 15]. However, few studies on ZnO/SnO_2 heterostructured nanocrystals have been reported although 1D ZnO or SnO_2 nanostructures have been studied extensively. Recently, nanomaterials have been

widely utilized to construct high-performance biosensors [16]. It is well known that the biosensing properties of nanomaterial-based biosensors closely associate with the nanomaterials' components, sizes, structures, and shapes [17–21]. Previous studies have indicated that, for composite nanomaterials with two or more components, one component usually amplifies the properties of the other components and even generates new properties [18, 22]. Moreover, these composite nanomaterials usually possess higher surface area, numerous nanometer-scale cavities, and highly active sites, which are very useful for proteins to sequester in the cavities or bind on the surface. At present, many papers on ZnO or SnO_2 nanomaterial-constructed biosensors have been published [19, 23, 24]. However, to the best of our knowledge, this is the first study showing that ZnO/SnO_2 heterostructured nanocrystals are utilized to immobilize proteins and construct electrochemical biosensors. In the present work, ZnO/SnO_2 heterostructured nanocrystals in which 1D SnO_2 nanocrystals grown on ZnO nanowires were fabricated by hydrothermal method. The ZnO/SnO_2 nanostructures were explored to build a biosensing platform by immobilizing hemoglobin (Hb) with chitosan (Chi). Meanwhile, the biological activity and electrochemical properties of the Hb entrapped in ZnO/SnO_2–Chi composite film were measured.

Experimental

Materials

Hb (MW 64,500, from bovine blood) and Chi were purchased from Sigma-Aldrich. The following analytical reagent-grade reagents were obtained from Guangdong Guanghua Chemical Reagent Co.: zinc acetate ($Zn(Ac)_2{\cdot}2H_2O$), sodium hydroxide (NaOH), ethanol (C_2H_5OH), tin chloride ($SnCl_4{\cdot}5H_2O$), heptane, hexanol, sodium dodecyl sulfate, sodium dihydrogen phosphate (NaH_2PO_4), disodium hydrogen phosphate (Na_2HPO_4), phosphoric acid (H_3PO_4), hydrogen peroxide (H_2O_2), concentrated hydrochloric acid (HCl), concentrated nitric acid (HNO_3), and high-purity nitrogen. All of the above reagents were used without further purification. Milli-Q water (>18.0 MΩ cm^{-1}) was used to prepare all aqueous solutions. All glassware used were washed with aqua regia and rinsed with >18.0 MΩ cm^{-1} water prior to use. A volume of 20 mM of phosphate buffer solution (PBS, pH 7.0) was prepared by mixing 39 mL 20 mM NaH_2PO_4 and 61 mL 20 mM Na_2HPO_4, and then various pH values of PBS were obtained through adjusting the PBS pH with a small quantity of 0.1 M H_3PO_4 or NaOH solutions.

Synthesis of ZnO/SnO_2 heterostructured nanomaterials

In a typical procedure for the synthesis of ZnO/SnO_2 heterostructured nanomaterials, 1 mmol $Zn(Ac)_2{\cdot}2H_2O$ and 10 mmol NaOH were first added into a Teflon-lined stainless steel autoclave, respectively. Then, 30 mL C_2H_5OH was also introduced into the autoclave. Finally, ZnO nanowires were obtained by heating the autoclave at 150 °C for 24 h, repeatedly centrifuging and washing the supernatant reaction mixture with milli-Q water and absolute ethanol several times, and drying at 80 °C for 4 h while the sample was cooled to room temperature; $SnCl_4{\cdot}5H_2O$ (0.1169 g) and NaOH (0.2667 g) were added into 2 mL H_2O under stirring, respectively. Then, heptane (10.0 mL), hexanol (3.0 mL), sodium dodecyl sulfate (1.44 g), and the freshly prepared ZnO nanowires (0.01 g) were added into the mixed solution and kept stirred for 3 min to form a homogeneous solution. After ultrasonication for 10 min, the mixture was transferred into a 25-mL Teflon-lined autoclave and heated to 180 °C for 24 h. When cooled to room temperature naturally, the resulting precipitates were collected by centrifugation, washed with absolute ethanol and milli-Q water several times, and dried at 80 °C for 5 h. SnO_2 nanocrystals were prepared using the same procedure except not adding 0.01 g ZnO nanowires.

Preparation of modified electrodes

A 3-mm-diameter glassy carbon (GC) electrode was polished with alumina (Al_2O_3) slurry of successively smaller particles (1.0, 0.3, and 0.05 μm in diameter, respectively). Then, the electrode was cleaned by ultrasonication in ultrapure water and ethanol, respectively. In a typical procedure for the preparation of the ZnO/SnO_2–Chi–Hb-modified electrode, the ZnO/SnO_2 nanostructures were firstly sonicated for 20 min, then equal volumes of 2 mg/mL ZnO/SnO_2 nanostructures, 2 mg/mL chitosan, and 4 mg/mL Hb were mixed. Next, 5 μL of the solution was cast onto the GC electrode surface with a 10-μL syringe. Finally, a uniform film electrode was formed through putting the as-prepared electrode overnight at room temperature and then using such for electrochemical investigations or storing at 4 °C in a refrigerator when not in use. For comparison, SnO_2–Chi–Hb/GC and ZnO/SnO_2–Chi/GC electrodes were also prepared. The suspension containing 2 mg/mL Hb, 1 mg/mL Chi, and 1 mg/mL SnO_2 nanocrystals was used to construct the SnO_2–Chi–Hb/GC electrode while 1 mg/mL ZnO/SnO_2 and 1 mg/mL Chi solution were employed to fabricate the ZnO/SnO_2–Chi/GC electrode.

Apparatus and measurements

Transmission electron microscopy (TEM) was performed with a Hitachi H-7500 microscope operated at 80 kV.

Scanning electron microscopy (SEM) and energy-dispersive X-ray spectroscopy (EDS) were carried out with a field-emission microscope (LEO, 1530 VP) operated at an accelerating voltage of 30 kV. X-ray diffraction (XRD) pattern was recorded on a powder sample using a D/max-IIIA (Japan) X-ray diffractometer with graphite monochromatized Cu Kα radiation (λ=0.15418 nm) ranging from 10° to 90°. UV–visible (UV–vis) absorption spectroscopy measurement was carried out with a U-3010 spectrophotometer (Hitachi, Japan). Electrochemical measurements were performed at room temperature using a CHI660 electrochemical workstation (CH Instru. Co., Shanghai, China). Electrochemical impedance spectroscopy spectra were acquired using an AUTOLAB advanced electrochemical system (Swiss). The measurements were based on a three-electrode system with the as-prepared film electrode as the working electrode, a platinum wire as the auxiliary electrode, and a saturated Ag/AgCl electrode as the reference electrode. Without special statement, 20 mM pH 7.0 PBS was used as the electrolyte in all experiments.

Results and discussion

Morphology and structure characterization of the ZnO/SnO_2 heterostructured nanomaterials

Figure 1 shows typical TEM and SEM images of SnO_2 nanocrystals and ZnO/SnO_2 heterostructured nanomaterials produced thus, respectively. As could be seen from Fig. 1a, c, the SnO_2 nanocrystals had average diameter and aspect ratio of ca. 82 nm and 3.1, respectively, and consisted of many short nanorods. In this system, the ZnO nanowires could be prepared through reacting among the Zn $(Ac)_2{\cdot}2H_2O$, NaOH, and C_2H_5OH precursors [25]. Using the ZnO nanowires, a tremendous quantity of well-aligned SnO_2 nanorods with average diameter and aspect ratio of 4 nm and 12, respectively, could be grown through adding $SnCl_4{\cdot}5H_2O$, NaOH, heptane, hexanol, and sodium dodecyl sulfate under hydrothermal atmosphere (Fig. 1b, d). To verify the component of the sample produced thus, EDS measurement was preformed. The Cu, C, and Au elements (Fig. 2) were from the copper grid and spurted Au made for the SEM sample. The appearance of the three elements Zn, Sn, and O indicated that the sample was probably ZnO/SnO_2 nanostructures.

To further investigate the components of the samples, XRD measurements were carried out. Figure 3 gives the XRD patterns of the SnO_2 nanomaterials and ZnO/SnO_2 heterostructured nanomaterials. It could be clearly seen from Fig. 3a that all diffraction peaks at 33.7°, 37.6°, 51.6°, 54.5°, 58.0°, 61.6°, 65.0°, 71.4°, and 78.5° could be

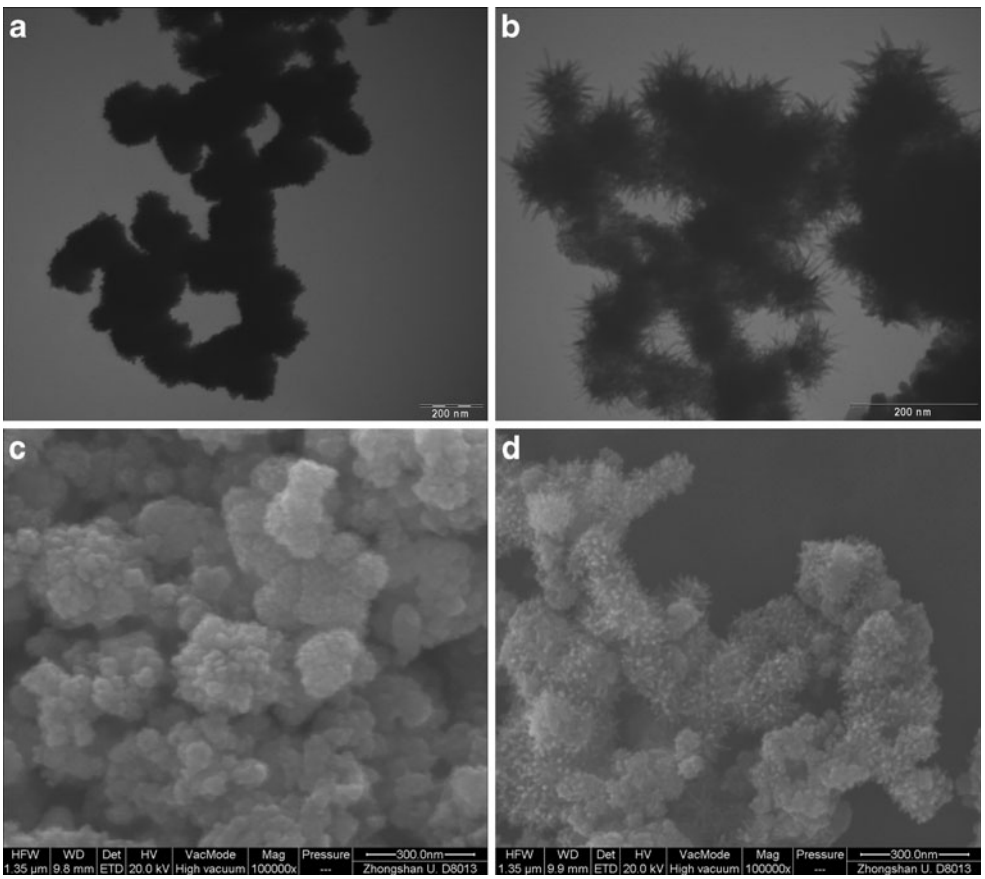

Fig. 1 **a**, **b** TEM and **c**, **d** SEM images of SnO_2 nanomaterials and ZnO/SnO_2 heterostructured nanomaterials produced thus, respectively

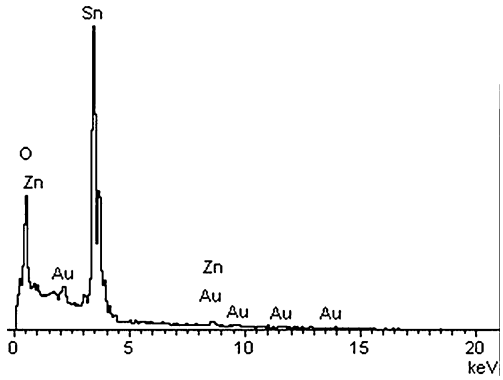

Fig. 2 EDS image of the ZnO/SnO_2 heterostructured nanomaterials prepared thus

indexed to (101), (200), (211), (220), (002), (310), (112), (202), and (231) planes of the tetragonal rutile structure of SnO_2 (JCPDS: 03–0439), respectively, demonstrating that the sample was pure SnO_2. Besides the diffraction peaks of the SnO_2, four new diffraction peaks, corresponding to (100), (002), (101), and (102) crystallographic planes, were also observed in Fig. 3b, which further demonstrated that the ZnO/SnO_2 heterostructured nanomaterials were formed and the secondary-grown SnO_2 nanorod branches and the primary ZnO nanowire substrates were highly crystallized.

Biocompatibility and electron transfer property characterization of the ZnO/SnO_2–Chi–Hb composite film

It is well known that UV–visible absorption is sensitive for determining the characteristic structure of redox proteins [26–29]. Previous studies have proved that the biological activity of heme proteins depend on the Soret absorption band position of heme because it can provide information on possible denaturation of heme proteins [30]. Figure 4 shows the UV–visible absorption spectra of the dry ZnO/SnO_2–Chi, Hb, and ZnO/SnO_2–Chi–Hb films. No UV–visible absorption peak of the dry ZnO/SnO_2–Chi film could be observed (curves a). An obvious UV–visible absorption peak at around 405 nm from dry Hb film could be clearly discerned, which was a characteristic Soret absorption band (curve c). When Hb was entrapped in the ZnO/SnO_2–Chi film (curve b), both peak position and intensity of the Hb spectrum were nearly invariable in comparison with that of pure Hb film, suggesting that the Hb still retained the essential feature of its native secondary structure in the ZnO/SnO_2–Chi–Hb film and had good biocompatibility with the ZnO/SnO_2 heterostructures.

Figure 5 displays Nyquist plots of different modified GC electrodes in pH 7.0 0.1 M KCl solution containing 5 mM $[Fe(CN)_6]^{3-/4-}$ (1:1). In the Chi-modified GC electrode (curve a), electron transfer resistance (R_{ct}) could be estimated to be about 183 Ω, implying that Chi was a good medium for electron transfer. When the ZnO/SnO_2 or SnO_2 nanomaterials were deposited, respectively, on the GC electrodes through cross-linking with Chi, a small increase of the interfacial resistance (about 643 Ω and 671 Ω, curves b and c) was observed, which was probably due to the spatial resistance between nanomaterials and the probe molecule, $Fe(CN)_6^{3-/4-}$. With further introducing Hb onto the modified electrodes, a significant increase in the interfacial resistance (about 10,021 and 20,710 Ω, curves d and e) was observed, indicating that Hb hindering the electron transfer pathway was successfully immobilized on the electrode surface. Nevertheless, the R_{ct} (about 10,021 Ω, curve d) of the ZnO/SnO_2-based electrode was much smaller than that (about 20,710 Ω, curve e) of the SnO_2-based electrode. The phenomenon indicated that the ZnO/SnO_2 nanostructures possessed better ionic conductivity and electron transfer property in comparison with the SnO_2 nanocrystals.

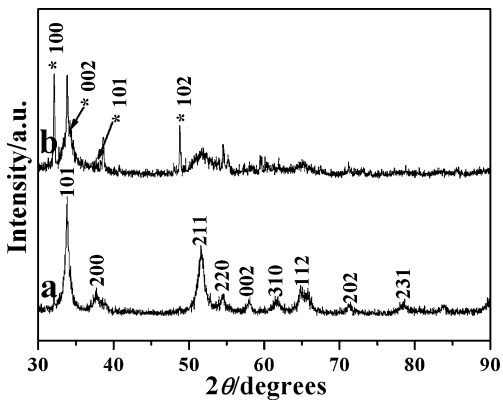

Fig. 3 XRD patterns of (*a*) SnO_2 nanocrystals and (*b*) ZnO/SnO_2 heterostructured nanomaterials prepared thus. The diffraction peaks marked with *asterisk* belong to those of ZnO

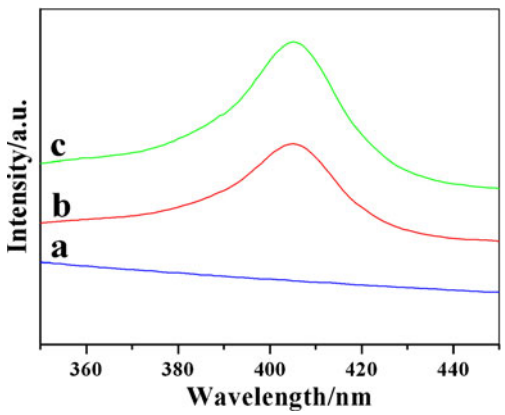

Fig. 4 UV–visible spectra of (*a*) dry ZnO/SnO_2–Chi, (*b*) ZnO/SnO_2–Chi–Hb, and (*c*) Hb film

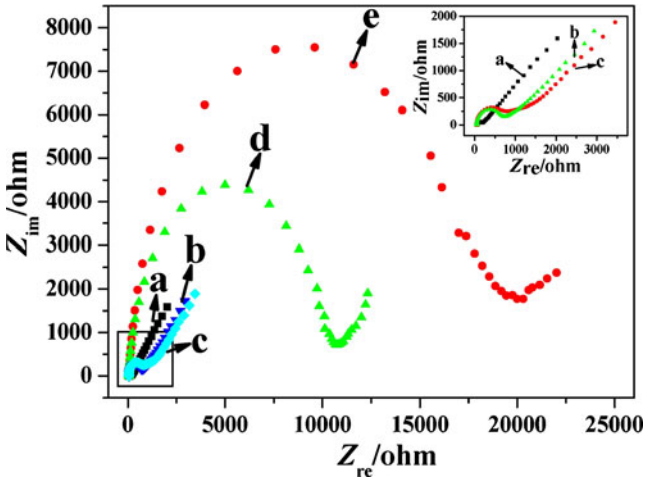

Fig. 5 Nyquist plots of different modified GC electrodes in 5 mM $[Fe(CN)_6]^{3-/4-}$ and 0.1 M KCl solution at pH 7.0 (*a*) Chi/GC, (*b*) ZnO/SnO_2–Chi/GC, (*c*) SnO_2–Chi/GC, (*d*) ZnO/SnO_2–Chi–Hb/GC, and (*e*) SnO_2–Chi–Hb/GC

Direct electrochemical property of the Hb immobilized ZnO/SnO_2-modified electrode

Cyclic voltammograms of GC electrodes modified with ZnO/SnO_2–Chi, SnO_2–Chi–Hb, and ZnO/SnO_2–Chi–Hb in 20 mM pH 7.0 PBS with scan rate of 0.2 Vs^{-1} are shown in Fig. 6. No redox peaks at the ZnO/SnO_2–Chi-modified electrode were observed (curve a), showing that the ZnO/SnO_2 heterostructures were not an electroactive material in the potential range. However, a pair of nearly reversible and well-defined peaks could be observed at the ZnO/SnO_2–Chi–Hb electrode (curve c), which could be attributed to the direct electron transfer between the Hb and the underlying electrode [31]. This indicated that the direct electron transfer for the Hb–Fe^{III}/Fe^{II} redox couple could be acquired at the ZnO/SnO_2-based biosensor. Interestingly, compared with the ZnO/SnO_2–Chi–Hb electrode, the redox peaks observed at the SnO_2–Chi–Hb electrode (curve b) were much smaller (less than twofold). The result indicated that the ZnO/SnO_2 heterostructures could greatly facilitate electron transfer between the Hb and the underlying electrode. The apparent formal potential $E^{\circ\prime}$ (estimated as $(E_{p,a}+E_{p,c})/2$, where $E_{p,a}$ and $E_{p,c}$ are the anodic and cathodic peak potentials, respectively) of the Hb entrapped in the ZnO/SnO_2–Chi composite film was found to be about −0.26 V, which was similar to those obtained in some previous studies [32–34]. The peak-to-peak separation (ΔE_p) was about 39 mV at 0.2 Vs^{-1}, which was much smaller than those reported for Hb in Fe_3O_4 nanoparticles [35] and meso-porous silica matrix [36] observed at the same scan rate. Such a smaller ΔE_p value revealed a more reversible behavior for faster electron transfer of the Hb immobilized in the ZnO/SnO_2 heterostructures. The enhanced redox currents and smaller ΔEp indicated that ZnO/SnO_2 heterostructures had better ionic conductivity and a faster electron transfer rate as compared with the SnO_2 nanocrystals.

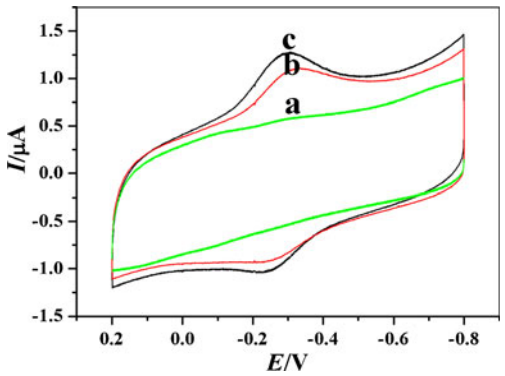

Fig. 6 Cyclic voltammograms of (*a*) ZnO/SnO_2–Chi/GC, (*b*) SnO_2–Chi–Hb/GC, and (*c*) ZnO/SnO_2–Chi–Hb/GC electrodes in 20 mM PBS (pH 7.0). Scan rate, 0.2 Vs^{-1}

Using Faraday's law, $Q=nFA\Gamma^*$ (Q, n, F, A, and Γ^* represent the quantity of charge, the number of electrons transferred, Faraday constant, effective electrode area, and surface average concentration of electroactive enzyme, respectively), the Γ^* of the electroactive Hb in the ZnO/SnO_2–Chi film film was estimated to be about 6.01×10^{-11} mol cm^{-2} (assuming a one-electron transfer reaction), which was three times higher than that of the theoretical monolayer coverage (about 1.9×10^{-11} mol cm^{-2}) [37]. This suggested that three layers of the self-assembly Hb molecules closest to the electrode participated in transferring electrons to the underlying electrode.

Figure 7 gives the cyclic voltammograms of the ZnO/SnO_2–Chi–Hb/GC electrode scanned at low and high scan

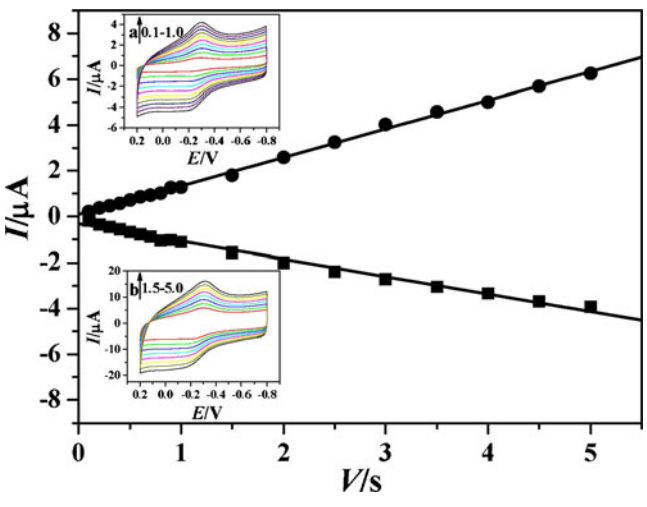

Fig. 7 Calibration plot of catholic (*curve a*) and anodic (*curve b*) peak currents vs. scan rates from 0.1 to 10 Vs^{-1} of ZnO/SnO_2–Chi–Hb/GC electrode. The *insets* are cyclic voltammograms measured with scan rates from 0.1 to 5.0 Vs^{-1}, respectively

rates, respectively. It could be seen that both reduction and oxidation peak currents increased linearly with increasing scan rates from 0.1 to 5 Vs^{-1}, indicating that all of the electroactive Hb in the film were reduced on the forwarded cathodic scan and the reduced Hb were then converted to the oxidized form on the reverse anodic scan. This result indicated that the ZnO/SnO_2 nanostructures provided a friendly microenvironment for the intercalated Hb to maintain its activity to a great extent and it was a surface-confined electrochemical process. The kinetic parameter k_s of the Hb immobilized on the ZnO/SnO_2-modified electrode was estimated using the model of Laviron [38]:

$$\log k_s/s^{-1} = \alpha\log(1-\alpha) + (1-\alpha)\log\alpha - \log[(\frac{RT}{nFv})/s] - \frac{\alpha(1-\alpha)nF\Delta E_p}{2.3RT}$$

where α, k_s, ΔE_p, n, R, T, and v mean charge transfer coefficient, heterogeneous electron transfer rate constant, peak separation, the number of electrons transferred, gas constant, absolute temperature, and scan rate, respectively. Taking α and v as 0.5 and 0.2 Vs^{-1}, the value of k_s was determined to be about 17.4 s^{-1}, suggesting a fast electron transfer process of Hb at the ZnO/SnO_2 nanostructure-modified electrode.

The influence of the solution pH on the electrochemistry behavior of Hb at the ZnO/SnO_2–Chi–Hb/GC electrode was also evaluated. Figure 8 gives the cyclic voltammograms of the ZnO/SnO_2–Chi–Hb/GC electrode in the solutions with different pH values. It was found that the direct electrochemistry of the ZnO/SnO_2–Chi–Hb/GC electrode intimately depended on solution pH and that stable and well-defined cyclic voltammograms could be observed in the pH range of 4.0–9.0. With an increase in the pH from 4.0 to 9.0, both the reduction and oxidation peaks shifted linearly to the negative, and thus the apparent formal potential also decreased. Moreover, all these voltammetric peak potentials switched among different pH values were reversible. The plot of the apparent formal potentials versus pH values is shown in the inset of Fig. 8. The linear dependence of $E^{\circ\prime}$ on pH suggested that the redox reaction, except for electron transfer, also accompanied proton transfer. The slope from the linear plot of $E^{\circ\prime}$ versus pH was around −49.6 mV/pH, which was close to the expected value of −58.0 mV/pH for a single proton transfer coupled to a reversible single electron transfer [39]. Therefore, the reaction could be represented as follows:

$$Hb\left[Heme\left(Fe^{III}\right)\right] + H^+ + e^- \rightleftarrows Hb\left[Heme\left(Fe^{II}\right)\right]$$

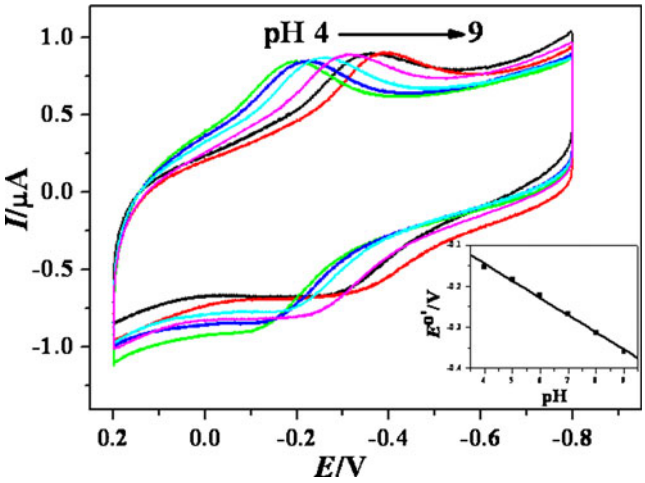

Fig. 8 Cyclic voltammograms of the ZnO/SnO_2–Chi–Hb/GC electrode with pH values of 4.0, 5.0, 6.0, 7.0, 8.0, and 9.0 (from *left* to *right*), respectively. *Inset*, plot of the apparent formal potentials versus pH values. Scan rate, 0.2 Vs^{-1}

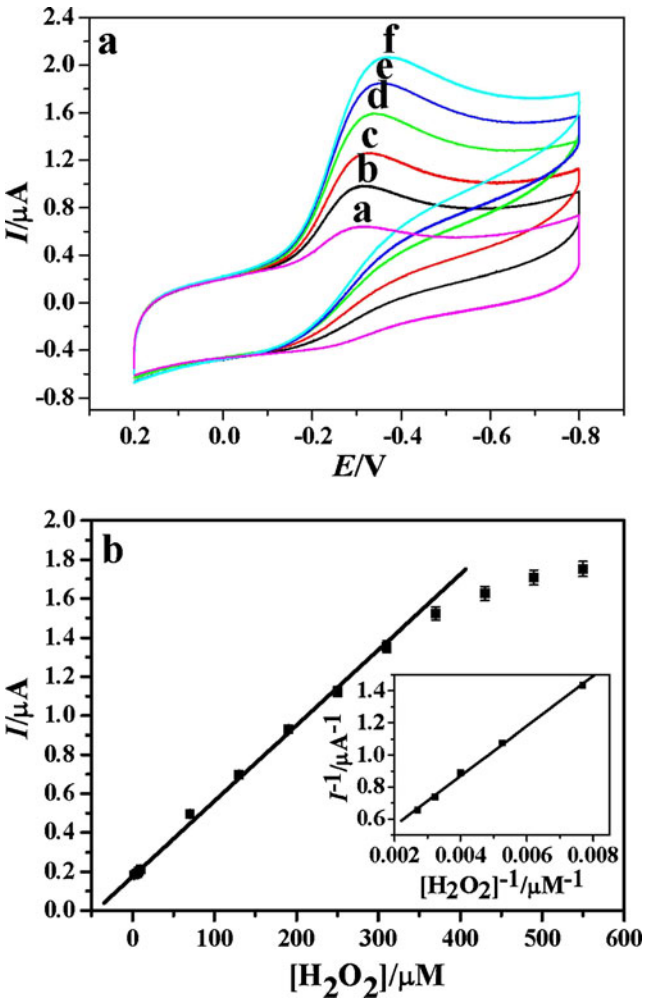

Fig. 9 **a** Bioelectrocatalysis of the ZnO/SnO_2–Chi–Hb biosensor towards H_2O_2 concentrations (μM): (*a*) 0, (*b*) 60, (*c*) 120, (*d*) 180, (*e*) 240, (*f*) 300. **b** Plot of the electrocatalytic current (I_{cat}) versus H_2O_2 concentration

Electrocatalytic property of the ZnO/SnO_2–Chi–Hb/GC electrode

In the biosensing system, the electrocatalytic property of the ZnO/SnO_2–Chi–Hb/GC electrode was studied through taking H_2O_2 as model. When H_2O_2 was added to 20 mM pH 7.0 PBS, the voltammograms of the ZnO/SnO_2–Chi–Hb/GC electrode showed a significant increase in the reduction peak current at about −0.30 V with the disappearance of the oxidation peak current, suggesting that a typical electrocatalytic reduction of H_2O_2 occurred (Fig. 9a). Figure 9b gives the plot of electrocatalytic currents (I_{cat}) versus H_2O_2 concentrations for the ZnO/SnO_2–Chi–Hb electrode in 20 mM pH 7.0 PBS. With increasing H_2O_2 concentration, the cathodic reduction current linearly increased initially and then tended to level off. The linear range was from 2.0×10^{-6} to 3.7×10^{-4} M (R=0.998, n=11), which was much wider than the reported value [40]. The detection limit of H_2O_2 at the ZnO/SnO_2–Chi–Hb/GC electrode was 4.6×10^{-7} M when signal-to-noise ratio (S/N) was 3. Biosensor sensitivity was associated with the biosensor's performance, biocompatibility, and stability, the enzyme electrode of which was calculated to be about 52.8 mA cm^{-2} M^{-1} through dividing the plot slope of the electrocatalytic current (I_{cat}) versus H_2O_2 concentration by the electrode area. Also, the sensitivities of the ZnO- and SnO_2-based biosensors were 10.6 and 8.4 mA cm^{-2} M^{-1}, respectively. Compared with the ZnO- and SnO_2-based biosensors, the higher sensitivity of the ZnO/SnO_2-based biosensor indicated that Hb entrapped in the composite film had excellent bioelectrocatalytic activity towards H_2O_2. The apparent Michaelis–Menton constant (K_M) could be estimated according to the Lineweaver–Burk equation [41]:

$$I_{ss}^{-1} = I_{max}^{-1} + K_M C^{-1} I_{max}^{-1}$$

where I_{ss}, I_{max}, and C stand for the steady-state response current after the addition of substrate, the maximum current measured under saturated substrate condition, and the bulk concentration of the substrate. In this biosensing system, K_M was estimated to be about 0.63 mM, which was smaller than that reported [42]. The relatively small K_M indicated that the Hb immobilized on the ZnO/SnO_2 heterostructures was of strong affinity to H_2O_2 and the ZnO/SnO_2–Chi–Hb/GC electrode had high catalytic efficiency to the reduction in H_2O_2 over a wide linear range with low detection limit.

Reproducibility and stability of the biosensor

The reproducibility of the biosensor was evaluated at a given concentration in the linear range by cyclic voltammetric measurements. The relative standard deviation (R.S.D.) of the biosensor response to 60 μM H_2O_2 for six successive measurements was 1.8%, indicating good reproducibility. To evaluate electrode-to-electrode reproducibility, six biosensors were prepared under the same and independent conditions. The R.S.D. of the biosensors was 2.9%, indicating good electrode-to-electrode reproducibility. The stability of the biosensor was studied by comparing the cyclic voltammetric peak currents of the Hb entrapped in the ZnO/SnO_2–Chi composite film with time intervals of 4 h. The decrease of the cathodic peak current of the biosensor immersed in PBS for 4 h was less than 3.1%, indicating that the biosensor possessed good stability. Moreover, the biosensor could retain 94.6% of its initial response after 15-day storage, suggesting good long-term stability. The good reproducibility and stability could be ascribed to the unique microstructure, shape, and good biocompatibility of the ZnO/SnO_2 heterostructures.

Conclusion

In summary, we have successfully fabricated ZnO/SnO_2 heterostructured nanomaterials by hydrothermal method in which the SnO_2 nanorods grew in quantity on the surface of ZnO nanowires. The ZnO/SnO_2 heterostructures with highly active sites were explored for the construct of direct electrochemical biosensor and have also been proved to be a good matrix for protein immobilization and electrochemical biosensor construction. Our results revealed that the Hb entrapped in the composite film still retained its essential secondary structure and the ZnO/SnO_2-based biosensor not only had enhanced direct electron transfer capacity but also displayed excellent electrocatalytic properties such as high sensitivity, wide linear range, low detection limit, good reproducibility and stability, and good long-term stability for the detection of H_2O_2. The ZnO/SnO_2 heterostructures are also expected to find potential applications in biomedical, food, and environmental analysis and detection.

Acknowledgements This work was supported by National Natural Science Foundation of China (No. 21173087) and the Open Project Program of State Key Laboratory of Pulp and Paper Engineering (No. 200904).

References

1. Gao AR, Lu N, Dai PF, Li T, Pei H, Gao XL, Gong YB, Wang YL, Fan CH (2011) Nano Lett 11:3974–3978
2. Gudiksen MS, Lauhon LJ, Wang J, Smith DC, Lieber CM (2002) Nature 415:617–620
3. Feng XM, Hu GQ, Hu JQ (2011) Nanoscale 2:2099–2117
4. Feng XM, Ruan FX, Hong RJ, Ye JS, Hu JQ, Hu GQ, Yang ZL (2011) Langmuir 27:2204–2210

5. Elangovan E, Ramamurthi K (2003) J Optoelectron Adv M 5:415–420
6. Law M, Kind H, Messer B, Kim F, Yang PD (2002) Angew Chem Int Ed 41:2405–2408
7. Park NG, Kang MG, Kim KM, Ryu KS, Chang SH (2004) Langmuir 20:4246–4253
8. Xiao LF, Li JP, Li Q, Zhang LZ (2010) J Solid State Electrochem 14:931–936
9. Hu JQ, Bando Y, Golberg D (2003) Chem Phys Lett 372:758–762
10. Duan JH, Yang SG, Liu HW, Gong JF, Huang HB, Zhao XN, Zhang R, Du YW (2005) J Am Chem Soc 127:6180–6181
11. Huang J, Matsunaga N, Shimanoe K, Yamazoe N, Kunitake T (2005) Chem Mater 17:3513–3518
12. Wang XD, Song JH, Li P, Ryou JH, Dupuis RD, Summers CJ, Wang ZL (2005) J Am Chem Soc 127:7920–7923
13. Sun SH, Meng GW, Zhang GX, Zhang LD (2007) Cryst Growth Des 7:1988–1991
14. Kotsikau D, Ivanovskaya M, Orlik D, Falasconi M (2004) Sens Actuators B 101:199–206
15. Cachet H, Vivier V, Toupance T (2004) J Electroanal Chem 572:249–255
16. Chen KI, Li BR, Chen YT (2011) Nano Today 6:131–154
17. Hu JQ, Yu Y, Guo H, Chen ZW, Li AQ, Feng XM, Xi BM, Hu GQ (2011) J Mater Chem 21:5352–5359
18. Ye C, Kong QC, Wu R, Hu JQ, Chen ZW, Li AQ (2010) Mater Lett 64:1720–1723
19. Feng XM, Liu YY, Kong QC, Ye JS, Chen XH, Hu JQ, Chen ZW (2010) J Solid State Electr 14:923–930
20. Hu JQ, Wang ZP, Li JH (2007) Sensors 7:3299–3311
21. Feng XM, Hu JQ, Chen XH, Xie JS, Liu YY (2009) J Phys D: Appl Phys 42:042001
22. Hu JQ, Wen ZH, Wang Q, Yao X, Zhang Q, Zhou JH, Li JH (2006) J Phys Chem B 110:24305–24310
23. Tu WW, Lei JP, Wang P, Ju HX (2011) Chem Eur J 17:9440–9447
24. Mahadeva SK, Kim J (2011) Sensor Actuat B- Chem 157:177–182
25. Hu JQ, Chen ZW, Xie JS, Ying Y (2008) J Phys D: Appl Phys 41:032004
26. Hu JQ, Chen Q, Xie ZX, Han GB, Wang RH, Ren B, Zhang Y, Yang ZL, Tian ZQ (2004) Adv Funct Mater 14:183–189
27. Hu JQ, Zhang Y, Liu B, Liu JX, Zhou HH, Xu YF, Jiang YX, Yang ZL, Tian ZQ (2004) J Am Chem Soc 126:9470–9471
28. Zhang L, Zhang Q, Li JH (2007) Adv Funct Mater 17:1958–1965
29. Kumar SA, Wang SF, Yeh CT, Lu HC, Yang JC, Chang YT (2010) J Solid State Electrochem 14:2129–2135
30. Huang H, Hu NF, Zeng YH, Zhou G (2002) Anal Biochem 308:141–151
31. King BC, Hawkridge FM, Hoffman BM (1992) J Am Chem Soc 114:10603–10608
32. Chen HJ, Dong SJ (2007) Biosens Bioelectron 22:1811–1815
33. Wang SF, Chen T, Zhang ZL, Shen XC, Lu ZX, Pang DW, Wong KY (2005) Langmuir 21:9260–9266
34. Zhou YL, Hu NF, Zeng YH, Rusling JF (2002) Langmuir 18:211–219
35. He YP, Sheng QL, Zheng JB, Wang MZ, Liu B (2011) Elentrochim Acta 56:2471–2476
36. Zhang L, Zhang Q, Li JH (2007) Electrochem Commun 9:1530–1535
37. Wang J (2005) Analyst 130:421–426
38. Laviron E (1979) J Electroanal Chem 101:19–28
39. Xie JS, Feng XM, Hu JQ, Chen XH, Li AQ (2010) Biosens Bioelectron 25:1186–1192
40. Kamin RA, Wilson GS (1980) Anal Chem 52:1198–1205
41. Huang YM, Zhang HL, Yu AM, Liu Y, Wu YW (2010) Sensor Lett 8:864–870
42. Chen XH, Hu JQ, Chen ZW, Feng XM, Li AQ (2009) Biosens Bioelectron 24:3448–3454